Chinese Physics Letters

EXPRESS LETTER

Exceptional-Point-Like Sensing near Hermitian Transmission Peak Degeneracies

Cite as: Jiangshan Tang *et al*. 2026 *Chin. Phys. Lett.* **43** 110402



Recommended Articles

Localization Dynamics at the Exceptional Point of Non-Hermitian Creutz Ladder
S. M. Zhang, T. Y. He, and L. Jin
Chin. Phys. Lett. **41**, (2024)

Topological Lasers and Exceptional Points in Parity-Time Symmetric Zero-Index Metamaterials
Qingjia Zhou, Qiuyi Long, Junhui Hu, Weijia Shao, and Yadong Xu
Chin. Phys. Lett. **42**, 120402 (2025)

Double Cavity Exceptional Point Enhanced Laser Cooling of Semiconductors
Haonan Chang, Feilong Song, and Jun Zhang
Chin. Phys. Lett. , (2026)

Generation of Multi-Order Sound Vortices via a Single Non-Hermitian Ring Cavity
Chen Liu, Tuo Liu, Zhongming Gu, and Jie Zhu
Chin. Phys. Lett. **43**, 031001 (2026)

Non-Hermitian Physics in Mesoscopic Electron Transport Through Coupled Quantum Dots
Yiyang Li, Jincheng Lu, Chen Wang, and Jian-Hua Jiang
Chin. Phys. Lett. **42**, 047303 (2025)

A series journal of Chinese Physical Society distributed by IOP Publishing

Chinese Physics Letters

Chin. Phys. Lett. **43** 110402 (2026)

EXPRESS LETTER

DOI: 10.1088/0256-307X/43/11/110402
CSTR: 32039.14.0256-307X.43.11.110402

Exceptional-Point-Like Sensing near Hermitian Transmission Peak Degeneracies

Jiangshan Tang(唐江山)[1,2,†], Longqi Xiao(肖隆奇)[1,†], Haodong Wu(吴浩东)[1,3], Yuwei Jing(景雨薇)[1], Han Zhang(张涵)[4], Yaping Ruan(阮亚平)[5], Wuming Liu(刘伍明)[6,7,*], Yan-Qing Lu(陆延青)[1,*], and Keyu Xia(夏可宇)[1,8,9,*]

[1]College of Engineering and Applied Sciences, National Laboratory of Solid State Microstructures, Nanjing University, Nanjing 210023, China
[2]College of Advanced Interdisciplinary Studies, National University of Defense Technology, Changsha 410073, China
[3]Xi'an Institute of Applied Optics, Xi'an 710065, China
[4]School of Physics, Nanjing University, Nanjing 210023, China
[5]Laboratory of Solar and Space Instruments, Nanjing Institute of Astronomical Optics and Technology, Chinese Academy of Sciences, Nanjing 210042, China
[6]School of Physics, Ningxia University, Yinchuan 750021, China
[7]Beijing National Laboratory for Condensed Matter Physics, Institute of Physics, Chinese Academy of Sciences, Beijing 100190, China
[8]Hefei National Laboratory, Hefei 230088, China
[9]Shishan Laboratory, Suzhou Campus of Nanjing University, Suzhou 215000, China

[†]These authors contributed equally to this work.
[*]Corresponding authors. Email: wmliu@iphy.ac.cn; yqlu@nju.edu.cn; keyu.xia@nju.edu.cn

Non-Hermitian sensing near exceptional points can exhibit a sublinear response to perturbations and thus promises sensitivity beyond conventional Hermitian sensors operating at diabolic points (DPs). Recent studies have further shown that the square-root readout can be attained near transmission peak degeneracy (TPD), where the splitting of spectral extrema, not the eigenvalues, is observed. However, in non-Hermitian platforms, the available sensitivity enhancement is fundamentally constrained by the divergent Petermann factor because of non-Hermitian eigenvector degeneracy and practically limited by the system complexity. Here, we experimentally demonstrate TPD-enhanced sensing of refractive-index change in a simple chiral Hermitian cavity. We show that the Hermitian transmission spectrum can also exhibit TPD-induced square-root splitting of spectral extrema while preserving eigenvector orthogonality. As a result, this Hermitian TPD-based sensor retains the response enhancement characteristic of non-Hermitian TPD sensing yet remains free from the Petermann-factor limit intrinsic to non-Hermitian systems, thereby enabling enhanced sensitivity. This work establishes a Hermitian route toward ultrasensitive sensing that surpasses the conventional DP sensor and provides a sensitivity advantage over non-Hermitian implementations when Petermann-factor-amplified noise is relevant.

Introduction

Exceptional-point-based sensors have attracted considerable interest because their sublinear response to perturbations offers a route beyond the linear-response limit of conventional Hermitian sensors operating near diabolic points (DPs). By exploiting the parity–time ($\mathcal{PT}$) symmetric phase transition, non-Hermitian sensors near exceptional points (EPs), where eigenvalues and eigenvectors simultaneously coalesce [1−6], have shown the essential advantages in response [7−24] and sensitivity [25−28] over a conventional Hermitian counterpart. Interplay of non-Hermitian physics and topology physics has further revealed EP-related topological structures [29−34] and also promises extremely high sensitivity [35]. Despite great advancements, the sensitivity of non-Hermitian sensors is technically constrained by the complexity of experimental implementation and fundamentally limited by the Petermann factor (PF), which originates from eigenvector nonorthogonality. It diverges near non-Hermitian degeneracies such as EPs [36−38] and amplifies noise in the sensing readout. This noise-amplification mechanism therefore raises a central question: whether one can retain the square-root response while avoiding eigenvector nonorthogonality.

Recent studies have addressed this question by exploring square-root readout at transmission peak degeneracy (TPD), where the splitting of spectral extrema serves as the sensing observable. This TPD regime has been theoretically analyzed [39] and subsequently realized in a landmark non-Hermitian accelerometer experiment [27], representing an important advance from EP-based response enhancement toward practical sensitivity improvement. At the same time, in those platforms, shifting the operating point from the EP to the TPD reduces, but dose not completely eliminate, the noise amplification associated with eigenvector nonorthogonality. Here we demonstrate that TPD-enhanced sensing can be implemented in a purely Hermitian cavity, where the eigenmodes remain strictly orthogonal. This Hermitian realization preserves the square-root spectral extremum readout of TPD sensing while circumventing both the experimental complexity of gain–loss engineering and the PF divergence intrinsic to non-Hermitian TPD sensors. It thus extends the scope of TPD-based sensing beyond non-Hermitian platforms.

A conceptual comparison of the conventional Hermitian DP-based sensor, the non-Hermitian sensors, and our Hermitian TPD-based sensor is illustrated in Fig. 1. These sensors involve two coupled modes. The figure depicts the measured frequency separation as a system response χ in the $\delta-\eta$ parameter space (inset surfaces), where δ is half of the frequency detuning between the two modes, the perturbation-induced coupling strength η is proportional to the normalized perturbation ϵ ($\epsilon \ll 1$), the dynamic response R (blue curves), defined as the derivative of the response with respect to perturbation, i.e., $R = \partial\chi/\partial\epsilon$. The PF (red dashed curves) is also presented for four sensors for comparison. A coupled two-mode system, as a general model of a sensor, can measure a perturbation at a bias ϵ_b as the induced frequency separation of observable. Conventionally, a Hermitian two-mode sensor with a vanishing gain/loss contrast, $\Delta\kappa = 0$, operates at the DP where $\delta = 0$ and $\epsilon_b = 0$. For any perturbation, its eigenfrequency splitting follows an ϵ-dependence, $\Delta\nu = \mathrm{Re}[\nu_+] - \mathrm{Re}[\nu_-] \propto \epsilon$, as

Received 30 September 2026; accepted 3 October 2026; published 4 November 2026
© 2026 Chinese Physical Society and IOP Publishing Ltd. All rights, including for text and data mining, AI training, and similar technologies, are reserved.

Check for updates

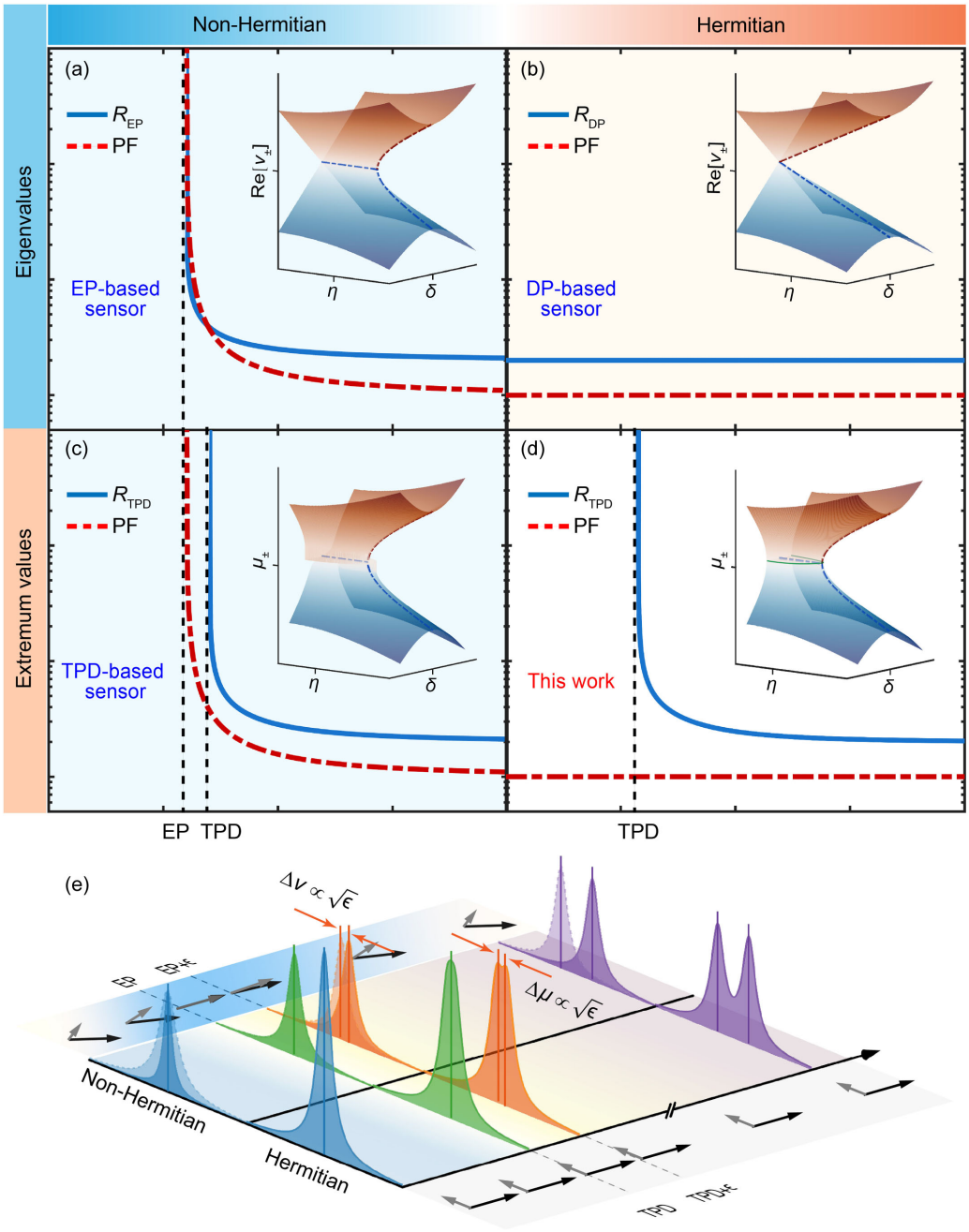


Fig. 1. Conceptual illustrations comparing sublinear response enhanced sensing in Hermitian and non-Hermitian systems. (a)–(d) Comparison of dynamic response R (solid blue curves) and PF (dashed red curves) for (a) the non-Hermitian EP-based sensor, (b) the Hermitian DP-based sensor, (c) the non-Hermitian TPD-based sensor, and (d) our Hermitian TPD-based sensor. The observable is the eigenfrequency splitting in the EP- and DP-based sensors, whereas it is the spectral-extremum splitting in the non-Hermitian and Hermitian TPD-based sensors. Insets in (a) and (b) show the real parts of the system eigenvalues of the non-Hermitian and Hermitian sensors in the $\eta-\delta$ parameter space, respectively. Insets in (c) and (d) depict the spectral extremum values with respect to their average value in the $\eta-\delta$ parameter space as (a) and (b). The black vertical dashed lines indicate the positions of the EP and the TPD, respectively. (e) Diagram comparing non-Hermitian EP-based sensor and our Hermitian TPD-based sensor. Left: an EP-based sensor with a panel illustrating nonorthogonal eigenvectors; the eigenmode transmission spectra are shown. Right: a Hermitian TPD-based sensor with a panel illustrating orthogonal eigenvectors; the overall transmission spectra are presented.

shown by the real parts Re[$\nu_\pm$] of the two complex eigenfrequencies in Fig. 1(b). This linear response implies a constant dynamic response, $R_{\rm DP}=\partial\Delta\nu/\partial\epsilon=$ const., and sets a fundamental limitation to the available sensitivity in the DP regime of a Hermitian sensor. By exploring the abrupt response at the EP associated with the $\mathcal{PT}$-symmetric phase transitions, a non-Hermitian sensor can tackle this ϵ-dependence limitation, see Fig. 1(a). Typically, it measures the eigenfrequency splitting, as shown in the left panel in Fig. 1(e). Below the EP, the transmission spectra of the two eigenmodes are located at the same frequency [Fig. 1(e)], implying vanishing eigenfrequency splitting; see Fig. 1(a). Slightly beyond the EP, $\eta(\epsilon_{\rm b})\gtrsim\eta_{\rm EP}$, the eigenfrequency splitting $\Delta\nu$ follows a $\sqrt{\epsilon}$-dependence for the on-resonance case $\delta=0$; see Fig. 1(e) and the inset in Fig. 1(a). Therefore, the dynamic response (blue curve) is enhanced by a divergent factor $\propto 1/\sqrt{\epsilon}$ compared to a conventional Hermitian sensor, as shown in Fig. 1(a). Well above the EP, the splitting is large, approaching a linear dependence on the perturbation. Because of this remarkably enhanced dynamic response, non-Hermitian sensors have the potential

to achieve unprecedented sensitivity overwhelming the conventional Hermitian counterpart [7,8]. Despite of some debates [40,41], this fundamental advantage of non-Hermitian sensors in sensitivity has been predicted by beautiful theories [7,8,42−44].

The sensitivity is more critical than the response for a sensor. It is crucially dependent on both the dynamic response and the noise in measurements [45,46]. The enhanced dynamic response has been successfully demonstrated in the gain–loss non-Hermitian sensors [10−13]. In these active systems, one mode is amplified to balance the loss of the other. Inevitably, the strong gain adds the dominant noise to the system. Because of the eigenvector coalescence, as indicated in Fig. 1(e), noise in a non-Hermitian sensor can be amplified to the same extent as its dynamic response by a divergent PF at the EP; see the red dashed curve in Fig. 1(a). This large PF imposes constraints on real sensitivity enhancement and can compensate the sensitivity improvement in the worst case [36,37]; see the red dashed curve. This PF problem of a non-Hermitian sensor is partly tackled by measuring the frequency splitting near the TPD, where the spectrum starts to splits to a doublet-peak profile [27,39]; see Fig. 1(c). The inset of Fig. 1(c) shows the peak positions $\mu_{\pm}$ of the transmittance spectra of a gain–loss non-Hermitian sensor. Intriguingly, the $\sqrt{\epsilon}$-dependence response is obtained near the TPD. Because the TPD slightly shifts away from the EP [27,39], the dynamic response is enhanced by a larger factor than the noise near the TPD. The PF-amplified noise is thus partly suppressed and a threefold enhancement is achieved for the sensitivity. A passive non-Hermitian sensor exhibits an important advantage over its active counterpart because it completely avoids the strong gain-induced noise; it achieves faithful sensitivity enhancement [25,26]. Nevertheless, the PF problem remains to be overcome and thus severely limits the available sensitivity enhancement because the intrinsic non-Hermitian degeneracy persists. Despite being highly demanded, it remains an outstanding challenge to develop a new sensing scheme that attains EP-like sensitivity enhancement without the PF limit.

The concept of our Hermitian TPD-enhanced sensor is depicted in Fig. 1(d) and is experimentally demonstrated in this work. The two modes equally decay with the same rate. Unlike the DP-based sensor observing the eigenfrequency splitting, our Hermitian TPD-based sensor measures the extremum separation of transmittance spectrum, $\Delta\mu$; see the right panel in Fig. 1(e). Below a bias level that $\eta(\epsilon_b) \le \eta_{\mathrm{TPD}}$, the transmission is a single peak. At η_{TPD}, the transmission shows a plateau profile. Slightly biased above this point, the spectral-extremum splitting (SES) increases rapidly with the perturbation. The inset in Fig. 1(d) shows the positions of two peaks of the transmission, $\mu_{\pm}$, versus the detuning and the perturbation. The two peaks locate at opposite sides of a spectral dip. The SES, defined as $\Delta\mu = \mu_+ - \mu_-$, displays a transition from a linear dependence to a square-root dependence on the perturbation at η_{TPD}. Comparing to the DP-based sensor, the dynamic response is enhanced by a factor of $\sqrt{\epsilon}$ near the TPD. In stark contrast to EP-based sensors and non-Hermitian TPD-based sensors, the eigenvectors of this Hermitian TPD-based sensor are intrinsically orthogonal [see the right panel of Fig. 1(e)], and therefore the PF remains unity under varying perturbation [see the red dashed line in Fig. 1(d)], thoroughly overcoming the divergent-PF problem. Generally, EP-based sensors, non-Hermitian TPD-based sensors, and our Hermitian TPD-based sensors are enabled by their respective singularities.

Experimental Setup

The experimental setup of this TPD-enhanced Hermitian sensor is illustrated in Fig. 2(a) [see Section 1 and Fig. S1 in the Supplementary Materials (SM) for details of this setup]. Basically, the sensor is a chiral Fabry–Pérot cavity embedded with a magneto-optical (MO) crystal. The cavity is made from two mirrors with equal reflectivity of 99.5%. The effective length of the cavity is $L_c = 80$ mm. The MO medium is a (111)-cut cylindrical terbium gallium garnet (TGG) crystal, made by the company (Model TGG-D3.5-20, Zhizhuo Optoelectronics Technology Co., Ltd., China). The refractive index of the TGG crystal is $n_s \approx 1.95$, corresponding to a relative dielectric constant of $\varepsilon_s = n_s^2 \approx 3.8$. The length of the crystal is $L_{\mathrm{MO}} = 20$ mm and its diameter is 3 mm, yielding a medium duty ratio of $\xi = L_{\mathrm{MO}}/[L_c + (\varepsilon_s - 1)L_{\mathrm{MO}}] \approx 14.7\%$. An anti-reflection dielectric film with equal transmittance of 99.7% is coated on each end facet of the TGG crystal to reduce cavity-mode loss. An electric coil surrounding the MO crystal is used to provide the external magnetic field $\boldsymbol{B}$. Due to the MO effect, $\boldsymbol{B}$ induces different refractive indices for right circularly polarized (RCP) and left circularly polarized (LCP) light. According to our measurement in Ref. [25], the Verdet constant of the TGG crystal is $C_v = 78.82$ rad/T·m.

A continuous-wave probe field with frequency ν from a laser (Toptica 795 nm) is input into the cavity via the left mirror. It is linearly polarized and the polarization is controlled by a polarizer. The polarization is along the direction at an angle θ with the horizontal plane. We can tune the driving to the horizontally polarized (HP) and vertically polarized (VP) modes by adjusting the polarization orientation θ.

Unlike the DP-based sensor, which detects eigenmode transmissions, we measure transmissions in the all-polarization (AP), HP, and VP spaces as interference between the RCP and LCP components. Based on the same Hermitian TPD configuration, the AP, HP, and VP channels provide experimentally accessible alternatives. Among them, the AP measurement is directly available without additional polarization selection. In contrast, the VP and HP measurements only require simple polarization projection. The transmitted light is first split into two paths by a beam splitter. A polarizing beam splitter is used again to divide the light in one path into the HP and VP modes. Light in the other path after the beam splitter is directly detected as the AP mode. The HP, VP, and AP transmitted fields are measured by three photoelectric detectors. Note that all of three fields compose of the RCP and LCP components associated with different phases and amplitudes. By sweeping the frequency ν of the probe field around the central wavelength $\lambda \sim 795$ nm, we can obtain the transmission spectra for measuring the perturbation. The SES is determined directly by the two maxima of the measured spectrum without any fitting function.

As conceptually depicted in Fig. 1, our Hermitian TPD-based sensor circumvents the PF amplification of noise, compared to a non-Hermitian sensor. To validate this concept, we examine the response and sensitivity enhancement by artificially adding intensity noise to both the probe field and the output field. We artificially add a strong intensity noise with a zero mean value to the probe field by randomly modulating the probe field via an acousto-optic modulator (AOM). In practice, the photoelectric detectors also causes background noise due to the imperfect quantum efficiency and dark electric currents. Simulations of this type of noise is performed by adding a noise field randomly modulated in its amplitude into the output fields via a beam splitter [47] (see details in the SM).

Theory

The Fabry–Pérot cavity supports two optical modes: the HP and VP modes, denoted as $\hat{a}_{\mathrm{H}}$ and $\hat{a}_{\mathrm{V}}$. We use ν_{H} and ν_{V} to denote their resonance frequencies, respectively. The left and right mirrors cause external decay rates $\kappa_{\mathrm{H}}^{\mathrm{ex}}$ and $\kappa_{\mathrm{V}}^{\mathrm{ex}}$ for the HP and VP modes, respectively. Here, the external decays via the input and output mirrors are assumed to be equal for simplicity such that $\kappa_{\mathrm{H}}^{\mathrm{ex}} = \kappa_{\mathrm{V}}^{\mathrm{ex}} = \kappa^{\mathrm{ex}}$. Considering the intrinsic losses $\kappa_{\mathrm{H}}^{\mathrm{in}}$ and $\kappa_{\mathrm{V}}^{\mathrm{in}}$, we respectively denote the total losses of the HP and VP modes as $\kappa_{\mathrm{H}} = 2\kappa^{\mathrm{ex}} + \kappa_{\mathrm{H}}^{\mathrm{in}}$ and $\kappa_{\mathrm{V}} = 2\kappa^{\mathrm{ex}} + \kappa_{\mathrm{V}}^{\mathrm{in}}$. These HP and VP eigenmodes are linearly polarized and degenerate in resonance frequency (such that $\nu_{\mathrm{H}} = \nu_{\mathrm{V}} = \nu_0$) and in dissipation (such that $\kappa_{\mathrm{H}} = \kappa_{\mathrm{V}} = \kappa$), leading to vanishing detuning $\delta = 0$ and gain/loss contrast $\Delta\kappa = 0$.

A magnetic field $\boldsymbol{B}$ along the axis of TGG crystal can induce an interaction between the modes $\hat{a}_{\mathrm{H}}$ and $\hat{a}_{\mathrm{V}}$ with a strength $g = \varepsilon_s \xi C_v \nu_0 / k_s$ [25], where k_s is the wavenumber of light in the MO medium that $k_s = 2\pi n_s/\lambda$, and B is the amplitude of the magnetic

field. We assume g to be real, as its imaginary part is at least two orders of magnitude smaller [25]. Then, the system is governed by the Hamiltonian:

$$H = \begin{bmatrix} \nu_0 - \mathrm{i}\kappa & \mathrm{i}gB \\ -\mathrm{i}gB & \nu_0 - \mathrm{i}\kappa \end{bmatrix}. \tag{1}$$

Thus, this MO-induced chiral Fabry–Pérot cavity is a Hermitian two-mode sensor. It allows the DP- and TPD-based measurements and thus facilitates comparison.

The MO-induced interaction converts the eigenmodes from linear polarization to circularly polarization such that $\hat{a}_+ = (\hat{a}_\mathrm{H} + \mathrm{i}\hat{a}_\mathrm{V})/\sqrt{2}$ and $\hat{a}_- = (\hat{a}_\mathrm{H} - \mathrm{i}\hat{a}_\mathrm{V})/\sqrt{2}$. The refractive index of the MO medium changes to $n_\mathrm{R} = n_\mathrm{s}(1 + C_\mathrm{v}B/2k_\mathrm{s})$ for the RCP eigenmode $\hat{a}_+$ and $n_\mathrm{L} = n_\mathrm{s}(1 - C_\mathrm{v}B/2k_\mathrm{s})$ for the LCP one $\hat{a}_-$, yielding a difference of $\Delta n = n_\mathrm{s}C_\mathrm{v}B/k_\mathrm{s} \approx gB/n_\mathrm{s}\xi\nu_0$. This refractive-index difference causes the eigenfrequency splitting of the RCP and LCP eigenmodes, given by $\Delta\nu = 2gB = 2n_\mathrm{s}\xi\nu_0\Delta n$. In the RCP and LCP basis, $\hat{a}_+$ and $\hat{a}_-$, the Hermitian becomes $H' = [\nu_0 + gB - \mathrm{i}\kappa, 0; 0, \nu_0 - gB - \mathrm{i}\kappa]$.

The probe field drives the HP and VP modes with relative strengths $\cos\theta$ and $\sin\theta$. A DP-based sensor measures the splitting of the two eigenmode transmissions and yields a response $\Delta\nu = 2gB$ and a dynamic response $R_\mathrm{DP} = 2g$. This work focuses on the response and sensitivity enhancement of the Hermitian TPD-based sensor. We can find the position of the peaks, namely the spectral extremum, by calculating the zeros of the derivative of the transmission T with respect to the probe frequency. When $\theta = \pi/4$, the SES in the VP, AP, and HP spaces, as a response, are respectively given by

$$\Delta\mu = \begin{cases} \mathrm{Re}\left[2\sqrt{-(\kappa - gB)^2 + 2gB\sqrt{\kappa^2 + (\kappa - gB)^2}}\right] & \text{in the VP space,} \\ \mathrm{Re}\left[2\sqrt{-(\kappa^2 + g^2B^2) + 2gB\sqrt{\kappa^2 + g^2B^2}}\right] & \text{in the AP space,} \\ \mathrm{Re}\left[2\sqrt{-(\kappa + gB)^2 + 2gB\sqrt{\kappa^2 + (\kappa + gB)^2}}\right] & \text{in the HP space.} \end{cases} \tag{2}$$

Note that this expression becomes imaginary for $B < B_\mathrm{TPD}$, indicating the absence of two distinct spectral extrema in the single-peak regime. In this region, the measured SES is zero. The two peaks locate at $\mu_\pm = \nu_0 \pm \Delta\mu/2$. The SES exhibits a square-root dependence on the magnetic field B. This square-root response originates from a symmetry-protected bifurcation of the spectral lineshape. Near the resonance center, the transmission is locally symmetric with respect to the detuning $\Delta = \nu - \nu_0$, such that its local expansion contains only even-order terms,

$$T(\Delta) \approx T_0 + a(B)\Delta^2 - b(B)\Delta^4 + O(\Delta^6). \tag{3}$$

Here $b(B) > 0$, and $O(\Delta^6)$ denotes higher-order even terms starting from the sixth order in Δ. The coefficient $a(B)$ characterizes the curvature of the central spectral feature. At $B = B_\mathrm{TPD}$, $a(B) = 0$, such that the single peak becomes locally flat. Beyond this point, the sign change of $a(B)$ drives the emergence of two symmetric extrema. From the extremum condition $\partial T/\partial\Delta = 0$, one obtains $\Delta_\pm \approx \pm\sqrt{a(B)/2b(B)}$. Since $a(B) \propto B - B_\mathrm{TPD}$ to leading order near the TPD, the extremum splitting follows $\Delta\mu \propto \sqrt{B - B_\mathrm{TPD}}$. This local symmetry also implies that uniform amplitude fluctuations do not shift the spectral-extremum positions to first order and therefore leave the SES unchanged. Practical perturbations, such as residual detuning and multimode coupling effects, may shift the TPD position, but the local square-root bifurcation structure remains preserved (see Sections S7.1 and S7.2 in SM for details).

This symmetry-protected bifurcation can also be understood from the interplay between linear eigenfrequency splitting and finite Lorentzian linewidth broadening. The MO interaction induces a linear splitting of the two eigenfrequencies, while the finite linewidth causes the corresponding resonances to overlap in the measured transmission spectrum. When the eigenfrequency splitting becomes comparable to the linewidth, the curvature of the central transmission peak changes sign, leading to the emergence of two spectral extrema through a bifurcation process. This physical picture provides an intuitive understanding of the origin of the square-root SES near the TPD. The possibility of higher-order TPD responses and the extension of this mechanism to non-Lorentzian spectra are further discussed in Sections S7.3 and S7.4 of the SM.

The observed sublinear splitting of the spectral extrema is distinct from the enhanced response achieved in other Hermitian resonant sensing schemes. Fano-resonance-based sensors exploit interference-induced asymmetric lineshapes with large spectral slopes. Bound-state-in-the-continuum (BIC) sensors rely on quasi-BIC resonances with large quality factors and enhanced light–matter interactions [48–57]. These schemes enhance sensitivity mainly by sharpening the resonance feature, equivalently increasing the quality factor. However, their sensing signal is typically extracted from the spectral shift of a resonance peak. This shift is linearly dependent on the perturbation to first order. By contrast, our Hermitian TPD mechanism uses the splitting of spectral extrema in the projected transmission as the sensing observable. The splitting follows a square-root scaling near the TPD. This sublinear response, combined with the absence of the PF penalty, defines a distinct Hermitian sensing mechanism that complements Fano- and BIC-based resonant sensors.

The dynamic responses, defined as $R_\mathrm{TPD} = \partial\Delta\mu/\partial B$, show discontinuous transition in all three measurement scenarios. Below the TPD, the response $\Delta\mu$ is null. At B_TPD, the splittings display an abrupt transition from null to a square-root dependence on the magnetic perturbation for $B > B_\mathrm{TPD}$, and thus on the refractive-index difference Δn, as conceptually illustrated in Fig. 1(d). By setting $\Delta\mu = 0$, we find the TPD at $gB_\mathrm{TPD} \approx 0.23\kappa$ in the VP measurement, $gB_\mathrm{TPD} = \sqrt{3}\kappa/3$ in the AP measurement, and $gB_\mathrm{TPD} \approx 0.77\kappa$ in the HP measurement.

Notably, the TPD position exhibits a different dependence on the polarization orientation θ. It is independent of θ in the AP measurement, while it shows complicated dependence on θ in the VP and HP cases, see Fig. 2(b). At $\theta = \pi/4$, the TPD appears first in the VP, then in the AP, and finally in the HP measurements. This channel dependence follows naturally from the polarization-projection nature of the readout. Each measurement channel projects the circularly polarized eigenmodes onto a specific linear polarization basis. Because the projected amplitudes and their interference differ among the three channels, the curvature of the central spectral feature reaches zero at different magnetic field values. The AP detector receives balanced contributions from both circular components, yielding a θ-independent TPD. The multiple B_TPD values in the VP and HP channels arise from the non-monotonic polarization-dependent bifurcation condition of the projected transmission spectrum. Below, we experimentally examine the TPD-enhanced response and sensitivity at these three TPDs (see SM for details in experimental setups).

The more important sensitivity S is defined as the ratio of measurement uncertainty or noise σ to the dynamic response R within the total measurement τ, namely $S = \sigma/R\sqrt{\tau}$ [58]. In a gain–loss non-Hermitian sensor operating near the EP, the total noise basically includes five contributions arising from various sources. Its power can be written as

$$\sigma_\mathrm{EP} = \sqrt{\mathcal{PF}^2 \times (\sigma_\mathrm{gain}^2 + \sigma_\mathrm{shot}^2 + \sigma_\mathrm{cl}^2) + R_\mathrm{EP}^2\sigma_\mathrm{signal}^2 + \sigma_0^2}, \tag{4}$$

where the gain-induced noise σ_gain arises from spontaneous emission of the gain medium [38,42,59,60], and the shot noise σ_shot originates from quantum vacuum fields and the photon projection noise of the probe field [61]. These contributions represent the fundamental quantum noise. They are amplified by the EP-enhanced $\mathcal{PF}$, and $\mathcal{PF} \gg 1$ near the EP. In contrast, σ_cl models the classical noise in the probe field such as the intensity fluctuation. This noise couples into the system through the input ports and is also likewise amplified by the PF [38,61]. In our experiment, we directly measure the output but not via the heterodyne detection. Both the shot noise and classical noise cause the similar uncertainty in measurement. Therefore, by adding artificial noise in the probe intensity, we can simulate the shot noise. The

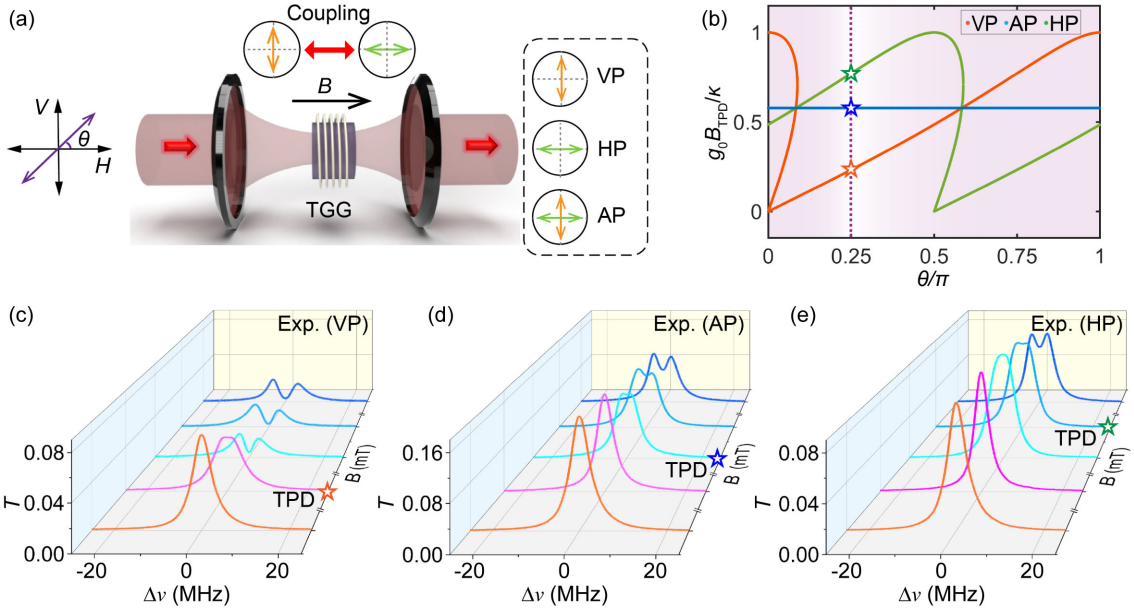


Fig. 2. Experimental setup and characterization. (a) Schematic of the experimental setup for the Hermitian TPD-enhanced sensor. (b) TPD position (B_{TPD}) of the simulated VP (orange), AP (blue), and HP (green) transmission spectra as a function of the incident polarization angle θ. The purple dashed line indicates the linearly polarized light incident at $\theta = 45^\circ$, as marked by the orange, blue, and green asterisks, respectively. (c)–(e) Experimental transmission spectra for the (c) VP, (d) AP, and (e) HP detections under different magnetic fields.

term σ_{signal} describes the noise homologous to the signal. As a signal-induced output, it is related to the dynamic response. For an artificial signal, this noise can be the uncontrollable fluctuation or side-effect of the signal, such as heating noise. For a real signal from environment, this contribution disappears. The final term σ_0 reflects the background noise imposed by technical constraints including the imperfect quantum efficiency and dark electric currents of the photoelectric detectors. In an active non-Hermitian sensor, the gain-related noise is dominant and thus compensate the sensitivity enhancement. In contrast, the passive non-Hermitian sensor is advantaged because the noise σ_{gain} is eliminated [25].

Remarkably, our Hermitian sensor contains no gain medium. Its eigenvectors are inherently orthogonal, completely avoiding the PF problem because $\mathcal{PF}$ remains unity. As a result, the total noise in a Hermitian sensor reduces to

$$\sigma_{\mathrm{DP/TPD}} = \sqrt{\sigma_{\mathrm{shot}}^2 + \sigma_{\mathrm{cl}}^2 + R_{\mathrm{DP/TPD}}^2 \sigma_{\mathrm{signal}}^2 + \sigma_0^2}. \tag{5}$$

In a non-Hermitian sensor, these two noise contributions are greatly amplified by the divergent PF near the EP. In our Hermitian TPD-based sensor, the noise amplification, defined as $G_\sigma = \sigma_{\mathrm{TPD}}/\sigma_{\mathrm{DP}}$, does not occur because the eigenmodes are orthogonal. Clearly, when the signal-related contribution is negligible, leading to $\sigma_{\mathrm{TPD}} \approx \sigma_{\mathrm{DP}}$, the sensitivity enhancement, evaluated as $G_{\mathrm{S}} = S_{\mathrm{DP}}/S_{\mathrm{TPD}} = G_{\mathrm{R}}/G_\sigma$, approaches to the response improvement G_{R}. This is the case for measuring a real signal. Notably, compared to a non-Hermitian sensor with a large PF and the strong gain-induced noise, our Hermitian TPD-based sensor can exhibit a much larger sensitivity enhancement even when two sensors display close dynamic response that $R_{\mathrm{EP}} \sim R_{\mathrm{TPD}}$. This is a key advantage of our Hermitian TPD-based sensor over a non-Hermitian sensor.

Results

The experimental transmission spectra for $\theta = \pi/4$ shown in Figs. 2(c)–2(e) confirm the depicted concept for the Hermitian TPD-based sensor in Fig. 1(e). For $\boldsymbol{B} < B_{\mathrm{TPD}}$, corresponding to a small Δn, the VP, AP, and HP transmissions exhibit singlet-peak structures, implying a null SES. This is because the eigenfrequency splitting is smaller than the eigenmode linewidths. At the TPD of B_{TPD}, the transmissions exhibit a plateau structure. As B further increases, Δn becomes bigger, causing a doublet-peak transmission. The spectral dip always appears at ν_0. The Hermitian TPD is first observed in the VP spectrum, secondly in the AP spectrum, and then in the HP spectrum, in good agreement with the theory [see the asterisks in Fig. 2(b)]. In Figs. 2(c) and 2(d), the transmission spectra far from TPDs show a slight asymmetry, which is caused by a small amount of magnetic-induced absorption within the cavity [25] (see details in SM).

The responses of the DP-based and our Hermitian TPD-based sensors are shown in Fig. 3(a). The DP-based sensor displays a linear response (purple), well fitted by a line. In contrast, all three responses in the VP, AP, and HP spaces exhibit an abrupt change from null to a square-root dependence on the magnetic field B, see the log–log plot in the inset. Above B_{TPD}, the experimental responses are well fitted by the theoretical results given in Eq. (2). The fitting parameter g takes the values of 0.90, 0.89, 0.89, and 0.90 MHz/mT for the DP sensor, the VP, AP, and HP measurements of the Hermitian TPD sensor, respectively. These close values indicate a good agreement between the experimental observations and theoretical predictions. The average value is $\bar{g} = 0.90$ MHz/mT. It means that a magnetic field of 1 mT can result in a refractive index difference of $\Delta n \approx 8.3 \times 10^{-9}$. Note that the SES in the VP measurement can surpass the eigenfrequency splitting in the DP-based sensor. This feature is not observed in the EP- and non-Hermitian TPD-based sensors.

In comparison with the DP-sensor, the response enhancement is clearly observed in the Hermitian TPD-based measurements and is evaluated as $G_{\mathrm{R}} = R_{\mathrm{TPD}}/R_{\mathrm{DP}}$, see Figs. 3(b)–3(d). Figure 3(b) shows the enhancement factors without artificially adding noise, reaching maximal values of $G_{\mathrm{R}} \approx 9.26$, 4.10, and 4.02 in the VP, AP, and HP measurements, respectively. As shown in Fig. 3(c) for artificially adding the intensity noise, the maximum enhancement factors in the VP, AP, and HP spaces are 9.42, 4.07, and 4.15, respectively. In simulation of strong background noise, the responses are enhanced by factors of 9.76 in the VP measurement, 3.96 in the AP, and 4.27 in the HP, respectively. The experimental results are well fitted by the same function derived from Eq. (2) in each measurement scenario (see Methods). As indicated by the theoretical model, the experimentally observed responses are similar in all three cases, meaning that they are independent of the noise.

Figure 4 compares the noise and the sensitivity of the Hermitian TPD- and DP-based sensors in three cases: no artificial noise (left

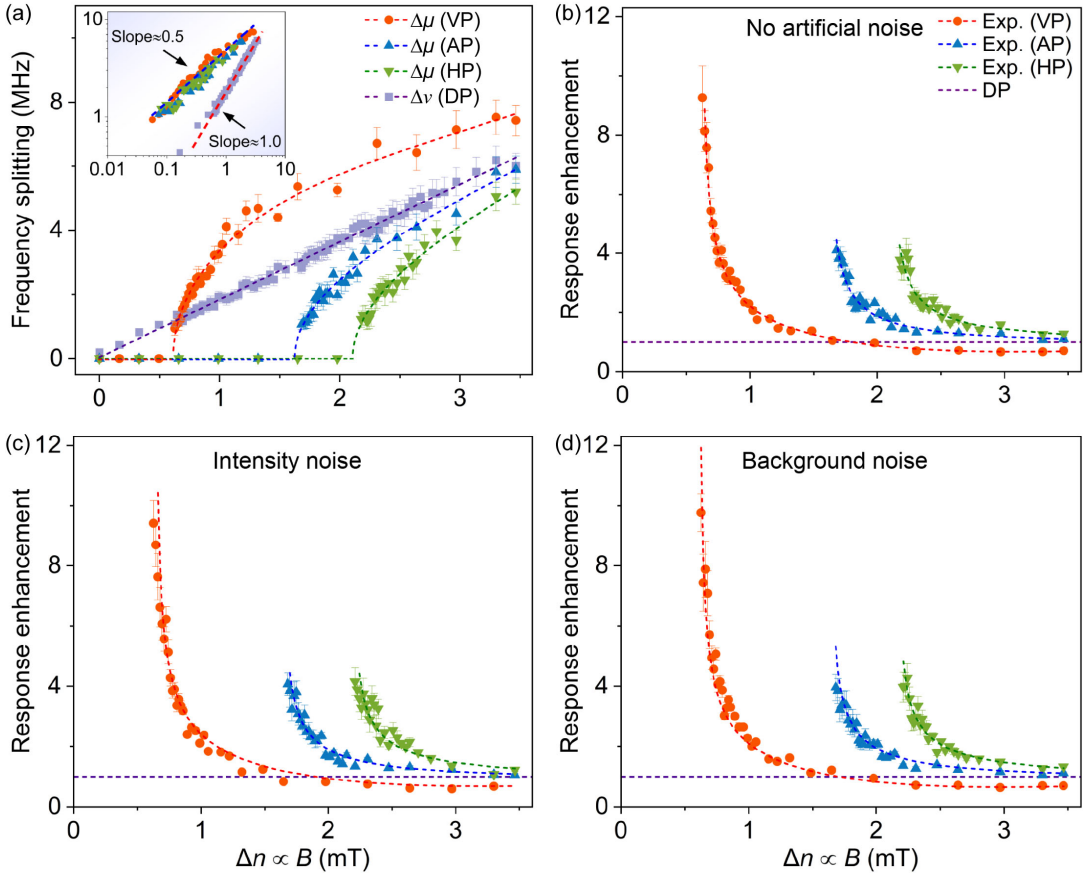


Fig. 3. Experimental observation and theoretical fitting of the Hermitian TPD-enhanced response to a refraction perturbation. (a) Eigenfrequency and spectral-extremum splittings versus the magnetic field. The insert shows the same data in a double-logarithmic fashion. (b)–(d) Response enhancement, G_R, of the Hermitian TPD sensor relative to the DP sensor (b) without additional noise, (c) with added laser intensity noise, and (d) with background noise. The discrete data points and curves represent the experimental and fitting results, respectively.

Table 1. Comparison of sensing metrics for DP, EP, non-Hermitian TPD, and Hermitian TPD sensors.

Scheme	Response	PF	Complexity[a]	Demonstrated G_S
DP sensor	$\propto \epsilon$	1	Low	1 [45]
Second-order EP sensor	$\propto \sqrt{\epsilon}$	$\gg 1$	High	Constrained by PF [10–13, 36–37, 62]
Non-Hermitian TPD sensor	$\propto \sqrt{\epsilon}$	>1	High	~3 in Ref. [27]
Hermitian TPD sensor	$\propto \sqrt{\epsilon}$	1	Low	~4.41 without added noise ~7.51 with intensity noise ~9.64 with background noise

[a]Low complexity implies passive degenerate cavity modes with tunable coupling. High complexity implies gain–loss engineering or dissipation imbalance.

panel), adding intensity noise (middle panel), and background noise (right panel). The lines and data for the DP-based sensor are presented for comparison. In the absence of artificial noise, the overall noise is amplified by a factor up to $G_\sigma \sim 3.7$ in the VP measurement, primarily attributed to the signal-related noise, $R_{\mathrm{TPD}}\sigma_{\mathrm{signal}}$. Correspondingly, the sensitivity enhancement G_S is about 4.10 [Fig. 4(d)]. In our experiment, the probe laser field is input to the sensor via an AOM for the purpose of enabling a reasonable comparison. The current noise in the AOM also causes fluctuation to the probe laser intensity. This noise is dominant over the contribution of $R_{\mathrm{TPD}}\sigma_{\mathrm{signal}}$ in the AP and HP measurements. As a result, the noise is slightly enhanced by ~1.2 times. Although the response enhancement is smaller in the AP and HP measurements, the noise level is lower than that in the VP measurement. Thus, the sensitivity is improved near the Hermitian TPD by a factor of $G_S \sim 4.41$, very close to the factor in the VP measurement. Without placing the AOM after the probe laser, the influence of the signal-related noise contribution becomes stronger. The noise amplification increases to about 1.60 near the Hermitian TPD in the AP and HP measurements, although the values are still smaller than that in the VP measurement (see SM).

We experimentally examine the prediction of the PF factor by adding intensity noise with zero mean value to the probe field via an AOM driven by a uniformly distributed random current (see SM for details). In our experiment, both the DP- and Hermitian TPD-based sensors directly measure the intensity of the transmitted fields. Thus, the intensity noise of the probe laser field has the same effect as shot noise and can therefore also simulate it. As shown in Fig. 4(b), when the intensity noise dominates other contributions, the noise amplification factors are close to unity in all three measurement scenarios, clearly confirming that $\mathcal{PF} = 1$. The sensitivity enhancement reaches larger values of 7.51, 5.49, and 7.40 in the VP, AP, and HP measurements, respectively.

In practice, the photoelectric detectors also add background noise due to the imperfect quantum efficiency and dark electric currents. To simulate background noise, we add a noisy laser field randomly modulated in amplitude to the output field via a beam splitter, as in

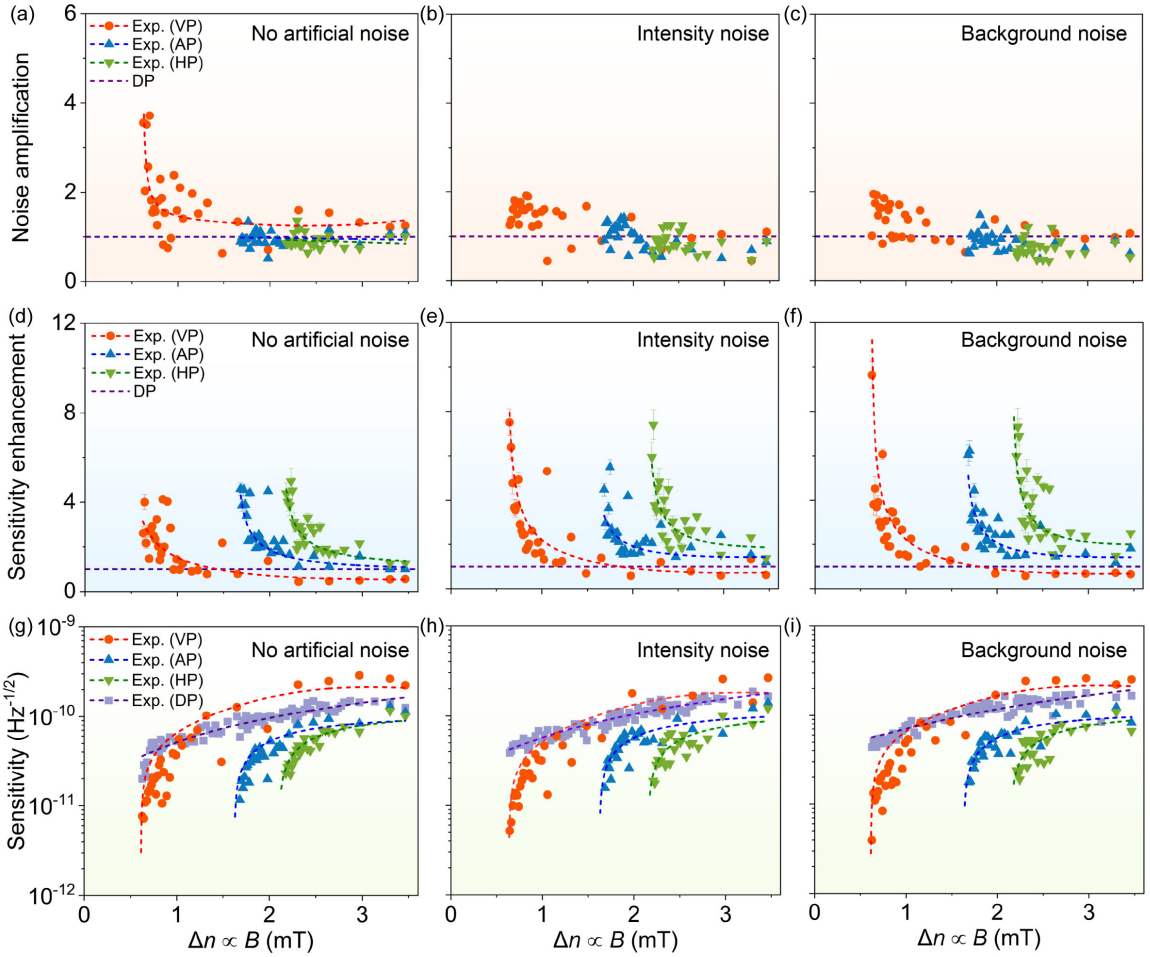


Fig. 4. Comparison of noise and sensitivity. Noise amplification (a)–(c), sensitivity enhancement (d)–(f), and sensitivity (g)–(i) of the Hermitian TPD-based sensors compared to the conventional DP-based sensor in the absence of artificial noise (left panel), with added laser intensity noise (middle panel), and with background noise (right panel). Orange, blue, and green data points correspond to the VP, AP, and HP measurements, respectively. Experimental data for the sensitivity, sensitivity enhancement and the noise amplification without artificial noise are fitted (see the following Methods section for details).

Ref. [47] (see details in SM). In this simulations, the artificial background noise is dominant. The noise amplifications display almost the same level as in the case of adding intensity noise [Fig. 4(c)]. The sensitivity enhancements are close to the response improvement factors [Fig. 4(f)], reaching a maximum of about 9.64 in the VP measurement.

To provide a quantitative comparison across different sensing schemes, we summarize in Table 1 the key metrics of the DP, EP, non-Hermitian TPD, and Hermitian TPD sensors. The Hermitian TPD sensor combines the square-root response characteristic of EP-based sensing with a PF of unity. Furthermore, its experimental complexity is comparable to that of a conventional DP sensor. Quantitatively, our scheme achieves a sensitivity enhancement $G_S \sim 4.4$ without added noise, $\sim$7.51 with added intensity noise, and $\sim$9.64 with background noise. These values substantially exceed the $\sim$3-fold enhancement reported for the non-Hermitian TPD sensor [27]. For the EP sensor, the divergent PF is known to fundamentally limit the net sensitivity gain [36,37,62].

Figures 4(g)–4(i) show the sensitivities. It is clear that the Hermitian TPD-based sensor exhibits better sensitivities in all measurement scenarios than the DP-based sensor. Particularly, the VP measurement achieves a refraction sensitivity dramatically superior to $10^{-11}/\sqrt{\text{Hz}}$.

Conclusions and Outlook

We have demonstrated Hermitian TPD-enhanced sensing of refraction in a chiral and passive optical system. This Hermitian TPD-based sensor exhibits a square-root response and achieves enhanced sensitivity relative to the DP-based counterpart. Remarkably, our sensor avoids the gain-induced noise and the PF amplification that can constrain the sensitivity of non-Hermitian sensors. The underlying mechanism can be extended to other coupled-mode platforms whose measured spectra support the required transmission-extremum bifurcation. Moreover, the local square-root bifurcation in Hermitian TPD sensing is protected by the symmetry of the transmission profile. Moderate mode asymmetry and multimode coupling may shift the TPD position, but do not necessarily eliminate the square-root response, as discussed in the SM. Our sensor is very simple but ultrasensitive to a small change of the refractive index.

The present work focuses on a passive Hermitian implementation. An active Hermitian extension provides an interesting direction for further enhancing the measurement sensitivity. If the gain medium does not fully compensate the cavity loss, the system remains effectively passive and is already covered by our present model. If identical net gain is introduced into the two modes, the system enters a gain–gain Hermitian regime. In this case, the square-root TPD response is still protected by the symmetry of the transmission profile, as verified in the SM. Such an active Hermitian TPD sensor may combine signal amplification with a unity PF, although amplification-induced instabilities, lasing dynamics, and nonlinear effects need to be carefully addressed in future studies.

Toward quantum-limited sensing, we have used classical intensity noise to examine the effect of shot noise. This treatment is equivalent in terms of how the noise couples into the measurement. This

provides a valid proof-of-principle demonstration of the PF-free sensitivity enhancement in the Hermitian TPD scheme. Nonetheless, a direct measurement of this enhancement against the fundamental quantum noise floor is a subject of further study. In addition, the sensitivity can be further improved by three to four orders if the laser central frequency is fast swept with an AOM. In combination with extra stabilization to reduce technical noise, this work may pave the way for testing the standard model and searching for axions [63,64], which cause a very tiny change to the refraction index of vacuum.

Methods

Hamiltonian and Transmission Spectrum

The system devices and parameters have been introduced in Section Theory. A linearly polarized laser field with frequency ν excites the MO Fabry–Pérot cavity with a drive amplitude α. Its polarization orientates at an angle θ to the horizontal plane. To facilitate the derivation of the transmission spectrum, we rewrite the system Hamiltonian in a quantum framework while explicitly including the external driving. In the frame rotating at frequency ν, the system Hamiltonian reads (we set the reduced Planck constant $\hbar = 1$)

$$\begin{aligned}\hat{H} = &-(\Delta-\delta)\hat{a}_{\mathrm{H}}^{\dagger}\hat{a}_{\mathrm{H}} - (\Delta+\delta)\hat{a}_{\mathrm{V}}^{\dagger}\hat{a}_{\mathrm{V}} + \mathrm{i}gB(\hat{a}_{\mathrm{H}}^{\dagger}\hat{a}_{\mathrm{V}} - \hat{a}_{\mathrm{V}}^{\dagger}\hat{a}_{\mathrm{H}}) \\ &+\mathrm{i}\sqrt{2\kappa^{\mathrm{ex}}}\alpha\cos\theta(\hat{a}_{\mathrm{H}}^{\dagger} - \hat{a}_{\mathrm{H}}) + \mathrm{i}\sqrt{2\kappa^{\mathrm{ex}}}\alpha\sin\theta(\hat{a}_{\mathrm{V}}^{\dagger} - \hat{a}_{\mathrm{V}}),\end{aligned} \tag{6}$$

where we have defined $\nu_0 = (\nu_{\mathrm{H}} + \nu_{\mathrm{V}})/2$, $\delta = (\nu_{\mathrm{H}} - \nu_{\mathrm{V}})/2$, and $\Delta = \nu - \nu_0$. In Eq. (6), the first two terms correspond to the free Hamiltonian, the third term describes the photon interaction, and the last two terms account for the external driving.

The Langevin equations of motion are given by

$$\frac{\mathrm{d}\hat{a}_{\mathrm{H}}}{\mathrm{d}t} = \mathrm{i}[\hat{H},\hat{a}_{\mathrm{H}}] + \mathcal{L}[\hat{a}_{\mathrm{H}}] = (\mathrm{i}\Delta_{\mathrm{H}} - \kappa_{\mathrm{H}})\hat{a}_{\mathrm{H}} + gB\hat{a}_{\mathrm{V}} + \sqrt{2\kappa^{\mathrm{ex}}}\alpha\cos\theta, \tag{7a}$$

$$\frac{\mathrm{d}\hat{a}_{\mathrm{V}}}{\mathrm{d}t} = \mathrm{i}[\hat{H},\hat{a}_{\mathrm{V}}] + \mathcal{L}[\hat{a}_{\mathrm{V}}] = (\mathrm{i}\Delta_{\mathrm{V}} - \kappa_{\mathrm{V}})\hat{a}_{\mathrm{V}} - gB\hat{a}_{\mathrm{H}} + \sqrt{2\kappa^{\mathrm{ex}}}\alpha\sin\theta. \tag{7b}$$

Here, $\mathcal{L}[\hat{o}] = \kappa(2\hat{o}^{\dagger}\hat{Q}\hat{o} - \hat{o}^{\dagger}\hat{o}\hat{Q} - \hat{Q}\hat{o}^{\dagger}\hat{o})$ with $\hat{o} = \{\hat{a}_{\mathrm{H}},\hat{a}_{\mathrm{V}}\}$ is the Lindblad superoperator acting on an arbitrary system operator $\hat{Q}$. Setting Eq. (7) to zero yields the system's steady-state solution:

$$\langle\hat{a}_{\mathrm{H}}\rangle = -\frac{\sqrt{2\kappa^{\mathrm{ex}}}\alpha[(\mathrm{i}\Delta + \mathrm{i}\delta - \kappa_{\mathrm{V}})\cos\theta - gB\sin\theta]}{(\mathrm{i}\Delta - \mathrm{i}\delta - \kappa_{\mathrm{H}})(\mathrm{i}\Delta + \mathrm{i}\delta - \kappa_{\mathrm{V}}) + (gB)^2}, \tag{8a}$$

$$\langle\hat{a}_{\mathrm{V}}\rangle = -\frac{\sqrt{2\kappa^{\mathrm{ex}}}\alpha[gB\cos\theta + (\mathrm{i}\Delta - \mathrm{i}\delta - \kappa_{\mathrm{H}})\sin\theta]}{(\mathrm{i}\Delta - \mathrm{i}\delta - \kappa_{\mathrm{H}})(\mathrm{i}\Delta + \mathrm{i}\delta - \kappa_{\mathrm{V}}) + (gB)^2}. \tag{8b}$$

The output fields follow from the input-output relations, $\hat{a}_{\mathrm{H,out}} = \sqrt{2\kappa^{\mathrm{ex}}}\hat{a}_{\mathrm{H}}$ and $\hat{a}_{\mathrm{V,out}} = \sqrt{2\kappa^{\mathrm{ex}}}\hat{a}_{\mathrm{V}}$. The VP, AP, and HP transmissions are defined as $T_{\mathrm{VP}} = |\langle\hat{a}_{\mathrm{V,out}}\rangle|^2/|\alpha|^2$, $T_{\mathrm{AP}} = |\langle\hat{a}_{\mathrm{H}}\rangle\boldsymbol{e}_{\mathrm{H}} + \langle\hat{a}_{\mathrm{V}}\rangle\boldsymbol{e}_{\mathrm{V}}|^2/|\alpha|^2$, and $T_{\mathrm{HP}} = |\langle\hat{a}_{\mathrm{H}}\rangle|^2/|\alpha|^2$, where $\{\boldsymbol{e}_{\mathrm{H}},\boldsymbol{e}_{\mathrm{V}}\}$ represent the HP and VP unitary vectors satisfying $\boldsymbol{e}_i\cdot\boldsymbol{e}_j = \delta_{i,j}$ with $i,j = \mathrm{H},\mathrm{V}$.

We first consider the Hermitian case, where $\kappa_{\mathrm{H}} = \kappa_{\mathrm{V}} = \kappa$. The eigenvalue of the system can be easily obtained as

$$\nu_{\pm} = \nu_0 - \mathrm{i}\kappa \pm \sqrt{g^2B^2 + \delta^2}. \tag{9}$$

From Eq. (9), one can plot a three-dimensional eigenvalue surface in the parameter space spanned by η and δ [Fig. 1(b)], where $\eta = gB$. For $\delta = 0$, the eigenfrequency splitting exhibits a linear dependence on the coupling strength gB.

The transmission of the Hermitian TPD-based sensor is given by

$$T(\Delta) = \begin{cases} \dfrac{(2\kappa^{\mathrm{ex}})^2[(gB\cos\theta - \kappa\sin\theta)^2 + (\Delta-\delta)^2\sin^2\theta]}{(g^2B^2 + \kappa^2 - \Delta^2 + \delta^2)^2 + 4\kappa^2\Delta^2} & \text{in the VP space,} \\ \dfrac{(2\kappa^{\mathrm{ex}})^2(g^2B^2 + \kappa^2 + \Delta^2 + \delta^2 + 2\Delta\delta\cos 2\theta)}{(g^2B^2 + \kappa^2 - \Delta^2 + \delta^2)^2 + 4\kappa^2\Delta^2} & \text{in the AP space,} \\ \dfrac{(2\kappa^{\mathrm{ex}})^2[(\kappa\cos\theta + gB\sin\theta)^2 + (\Delta+\delta)^2\cos^2\theta]}{(g^2B^2 + \kappa^2 - \Delta^2 + \delta^2)^2 + 4\kappa^2\Delta^2} & \text{in the HP space.} \end{cases} \tag{10}$$

By solving $\partial T/\partial\nu = 0$, one can construct the three-dimensional extremal surface of the transmission spectrum in the $\eta - \delta$ parameter space. The inset in Fig. 1(d) shows the extremal surface of the transmission spectrum in the AP space. It is worth noting that, when $\delta = 0$, there always exists a common extremum $\mu_{0,m} = \nu_0$ ($m = \mathrm{VP},\mathrm{AP},\mathrm{HP}$) independent of the parameter gB. However, as gB increases, two additional maxima emerge at $\mu_{+,m}$ and $\mu_{-,m}$. They symmetrically appear on both sides of $\mu_{0,m}$ in the transmission spectrum, forming a double-peak profile and indicating the onset of TPD. The number of extrema abruptly jumps from one to three, marking the TPD in the transmission spectrum. The TPD position differs in the VP, AP, and HP measurements.

In the VP measurement scenario, the maxima are

$$\mu_{\pm,\mathrm{VP}} = \begin{cases} \nu_0 \pm \sqrt{g^2B^2 - \kappa^2}, & \sin\theta = 0, \\ \nu_0 \pm \left[\dfrac{-(\kappa\sin\theta - gB\cos\theta)^2 + gB\sqrt{\mathcal{N}_{\mathrm{VP}}(\theta)}}{\sin^2\theta}\right]^{1/2}, & \sin\theta \neq 0, \end{cases} \tag{11}$$

where $\mathcal{N}_{\mathrm{VP}}(\theta) = g^2B^2 + 4\kappa^2\sin^2\theta - 4\kappa gB\sin\theta\cos\theta$. The extremum is a real number. When $\sin\theta = 0$, the TPD occurs at $gB_{\mathrm{TPD}} = \kappa$, where the number of extrema suddenly changes from one to three. When $\sin\theta \neq 0$, the TPD position is determined by numerically solving $\mu_{+,\mathrm{VP}} - \nu_0 = \mu_{-,\mathrm{VP}} - \nu_0 = 0$, as shown in the orange solid curve in Fig. 2(b).

In the HP measurement scenario, the maxima are

$$\mu_{\pm,\mathrm{HP}} = \begin{cases} \nu_0 \pm \sqrt{g^2B^2 - \kappa^2}, & \cos\theta = 0, \\ \nu_0 \pm \left[\dfrac{-(\kappa\cos\theta + gB\sin\theta)^2 + gB\sqrt{\mathcal{N}_{\mathrm{HP}}(\theta)}}{\cos^2\theta}\right]^{1/2}, & \cos\theta \neq 0, \end{cases} \tag{12}$$

where $\mathcal{N}_{\mathrm{HP}}(\theta) = g^2B^2 + 4\kappa^2\cos^2\theta + 4\kappa gB\sin\theta\cos\theta$. Similarly, for $\cos\theta = 0$, the TPD occurs at $gB_{\mathrm{TPD}} = \kappa$, while for $\cos\theta \neq 0$, its position is obtained by numerically solving $\mu_{+,\mathrm{HP}} - \nu_0 = \mu_{-,\mathrm{HP}} - \nu_0 = 0$, as indicated by the green solid curve in Fig. 2(b).

In the AP measurement scenario, the maxima are

$$\mu_{\pm,\mathrm{AP}} = \nu_0 \pm \sqrt{-(\kappa^2 + g^2B^2) + 2gB\sqrt{g^2B^2 + \kappa^2}}. \tag{13}$$

The TPD always occurs at $gB_{\mathrm{TPD}} = \kappa/\sqrt{3}$, independent of θ [see the blue solid line in Fig. 2(b)].

The SES in the Hermitian TPD-based sensor is defined as $\Delta\mu_m = \mu_{+,m} - \mu_{-,m}$ ($m = \mathrm{VP},\mathrm{AP},\mathrm{HP}$). It follows that the SESs in all three measurement scenarios scale as the square root of a perturbation ϵ near the TPD, corresponding to $gB = gB_{\mathrm{TPD}}$. In this work, we leverage this sublinear response for the Hermitian TPD-based sensing with enhanced response and sensitivity performance.

Next, we turn to the non-Hermitian case, where $\kappa_{\mathrm{H}} \neq \kappa_{\mathrm{V}}$, which allows for the emergence of EPs and markedly different spectral behavior compared with the Hermitian case. In our MO Fabry–Pérot cavity, this can be constructed either by introducing an additional loss contrast between the two cavity modes (e.g., using a liquid crystal [25]) or by adding gain for one of the modes. The eigenvalue of the non-Hermitian system is given by

$$\nu_{\pm} = \nu_0 - \mathrm{i}\frac{\kappa_{\mathrm{H}} + \kappa_{\mathrm{V}}}{2} \pm \sqrt{g^2B^2 + \left(\delta - \mathrm{i}\frac{\kappa_{\mathrm{H}} - \kappa_{\mathrm{V}}}{2}\right)^2}. \tag{14}$$

Equation (14) yields a three-dimensional eigenvalue surface in the

$\eta-\delta$ parameter space, as shown in Fig. 1(a). For $\delta=0$, the EP occurs at $gB_{\rm EP}=(\kappa_{\rm H}-\kappa_{\rm V})/2$. In contrast to Hermitian systems, near the EP, i.e., $gB=gB_{\rm EP}+\epsilon$, the eigenfrequency splitting exhibits a $\sqrt{\epsilon}$ dependence. This feature motivates the design of the EP-based sensing scheme [7,8].

In the non-Hermitian configuration, the transmission in the TPD-based sensor can be expressed as

$$T(\Delta)=\begin{cases}\dfrac{(2\kappa^{\rm ex})^2[(gB\cos\theta-\kappa_{\rm H}\sin\theta)^2+(\Delta-\delta)^2\sin^2\theta]}{\mathcal{D}(\Delta)} & \text{in the VP space,}\\ \dfrac{(2\kappa^{\rm ex})^2[\mathcal{N}_{\rm AP}(\theta)+\Delta^2+\delta^2+2\Delta\delta\cos 2\theta]}{\mathcal{D}(\Delta)} & \text{in the AP space,}\\ \dfrac{(2\kappa^{\rm ex})^2[(\kappa_{\rm V}\cos\theta+gB\sin\theta)^2+(\Delta+\delta)^2\cos^2\theta]}{\mathcal{D}(\Delta)} & \text{in the HP space,}\end{cases} \tag{15}$$

where $\mathcal{N}_{\rm AP}(\theta)=g^2B^2+\kappa_{\rm V}^2\cos^2\theta+\kappa_{\rm H}^2\sin^2\theta+gB(\kappa_{\rm V}-\kappa_{\rm H})\sin 2\theta$ and $\mathcal{D}(\Delta)=(g^2B^2+\kappa_{\rm H}\kappa_{\rm V}-\Delta^2+\delta^2)^2+[\Delta(\kappa_{\rm H}+\kappa_{\rm V})-\delta(\kappa_{\rm H}-\kappa_{\rm V})]^2$. Evidently, for $\kappa_{\rm H}=\kappa_{\rm V}=\kappa$, equation (15) simplifies to Eq. (10). By solving $\partial T/\partial\nu=0$, the extremal surface of the transmission spectrum in the AP space can be determined in the $\eta-\delta$ parameter space [Fig. 1(c)]. For $\delta=0$, the transmission spectrum shows a TPD [27,39]. Near this TPD, the extremum splitting also exhibits a square-root dependence on the perturbation ϵ. Although the non-Hermitian TPD-based sensor offers higher sensitivity than an EP-based sensor, its sensitivity is still constrained by the inherent PF problem, because the TPD slightly shifts away from the EP [27].

Spectral-Extremum Splitting Measurements

For each magnetic field, the transmission spectrum was measured by scanning the probe frequency over a 50 MHz window around the cavity resonance. Each spectrum contains 7221 frequency points, corresponding to an average frequency interval of about 6.92 kHz. To suppress random intensity fluctuations, each reported spectrum was obtained by averaging 30 consecutive scans under the same experimental condition. The SES was determined directly from the frequency difference between the two transmission maxima in the averaged spectrum, without using a fitting function to locate the extrema.

This direct-reading procedure is reliable for the present classical-probe measurements because the averaged spectra are smooth and the two maxima are clearly resolved, as shown in Figs. 2(c)–2(e). Importantly, the SES values extracted using this procedure agree well with the theoretical predictions over the experimentally accessible range, as shown in Fig. 3(a), providing an additional consistency check on the SES extraction. We emphasize that the theoretical fitting in Fig. 3(a) is performed after the SES values have been directly extracted and is not used to determine the positions of the transmission maxima.

Extremely close to the TPD, the two extrema merge into a nearly flat-top profile. In this regime, the SES is limited by finite frequency resolution and residual intensity fluctuations. As a result, SES values can be experimentally determined only when the two extrema become resolvable above the TPD.

The Response Enhancement Factors

The dynamic response of our Hermitian TPD-based sensor is defined as $R_{{\rm TPD},m}=\partial\Delta\mu_m/\partial B$ with $m={\rm VP,AP,HP}$. Accordingly, the dynamic responses for the VP, AP, and HP measurements are respectively

$$R_{\rm TPD,VP}=\frac{4g}{\Delta\mu_{\rm VP}}\left[(\kappa-gB)-\frac{(\kappa-gB)gB}{\sqrt{\kappa^2+(\kappa-gB)^2}}+\sqrt{\kappa^2+(\kappa-gB)^2}\right], \tag{16a}$$

$$R_{\rm TPD,AP}=\frac{4g}{\Delta\mu_{\rm AP}}\left[-gB+\frac{g^2B^2}{\sqrt{\kappa^2+g^2B^2}}+\sqrt{\kappa^2+g^2B^2}\right], \tag{16b}$$

$$R_{\rm TPD,HP}=\frac{4g}{\Delta\mu_{\rm HP}}\left[-(\kappa+gB)+\frac{(\kappa+gB)gB}{\sqrt{\kappa^2+(\kappa+gB)^2}}+\sqrt{\kappa^2+(\kappa+gB)^2}\right]. \tag{16c}$$

In contrast, the dynamic response of a conventional DP-based sensor is $R_{\rm DP}=2g$. The response enhancement is defined as $G_{R,m}=R_{{\rm TPD},m}/R_{\rm DP}$ ($m={\rm VP,AP,HP}$). Thus, we have

$$G_{R,\rm VP}=\frac{2}{\Delta\mu_{\rm VP}}\left[(\kappa-gB)-\frac{(\kappa-gB)gB}{\sqrt{\kappa^2+(\kappa-gB)^2}}+\sqrt{\kappa^2+(\kappa-gB)^2}\right], \tag{17a}$$

$$G_{R,\rm AP}=\frac{2}{\Delta\mu_{\rm AP}}\left[-gB+\frac{g^2B^2}{\sqrt{\kappa^2+g^2B^2}}+\sqrt{\kappa^2+g^2B^2}\right], \tag{17b}$$

$$G_{R,\rm HP}=\frac{2}{\Delta\mu_{\rm HP}}\left[-(\kappa+gB)+\frac{(\kappa+gB)gB}{\sqrt{\kappa^2+(\kappa+gB)^2}}+\sqrt{\kappa^2+(\kappa+gB)^2}\right]. \tag{17c}$$

Theoretically, these response enhancement approaches diverge near the TPD, implying the superiority of TPD-based sensors over DP-based ones in signal enhancement.

Fitting of Experimental Results

In this section, we present the theoretical fittings to the experimental results in the Hermitian TPD sensing without artificial noise as an example. The same method is used for the cases with artificial intensity noise and background noise. Firstly, based on Eq. (2), we fit the experimental SES data in Fig. 3(a) to extract the coupling strength g and the dissipation rate κ. The extracted g is 0.90 MHz/mT for the DP sensor, and 0.89, 0.89, and 0.90 MHz/mT for the VP, AP, and HP measurements of the Hermitian TPD sensor, respectively. The corresponding dissipation rates are 2.34, 2.50, and 2.46 MHz for the VP, AP, and HP cases. The close agreement of these values indicates consistency between the experimental observations and theoretical predictions. Therefore, in the subsequent data fitting, we use the extracted coupling strengths and dissipation rates for each measurement case. According to Eq. (17), the theoretical curves of response enhancement in the three measurement scenarios are presented in Fig. 3(b). Obviously, the theoretical model is in good agreement with the experimental results.

In our sensor, the sources of noise mainly consist of four parts, namely signal-related noise $\sigma_{\rm signal}$, shot noise $\sigma_{\rm shot}$, classical noise $\sigma_{\rm cl}$, and background noise σ_0, as presented in Eq. (5). Here, the signal-related noise contribution scales linearly with the magnetic field, namely $\sigma_{\rm signal}=\gamma_{\rm TPD(DP)}B$, with $\gamma_{\rm TPD(DP)}$ being the fitting parameter. The other three noise contributions are unaffected by the PF and denoted as $\sigma_{\rm other}$. We assume they are constant for the purpose of fitting. Thus, the expressions for noise amplification and sensitivity are

$$G_\sigma=\frac{\sigma_{\rm TPD}}{\sigma_{\rm DP}}=\sqrt{[\sigma_{\rm other}^2+(R_{\rm TPD}\gamma_{\rm TPD}B)^2]/[\sigma_{\rm other}^2+(R_{\rm DP}\gamma_{\rm DP}B)^2]}, \tag{18}$$

$$S_x=\frac{\sigma_x}{R_x}\sqrt{\tau}=\sqrt{\sigma_{\rm other}^2/R_x^2+\sigma_{\rm signal}^2}\sqrt{\tau} \tag{19}$$

with $x=\{{\rm TPD,DP}\}$ and τ being the total measurement time [58]. The sensitivity is enhanced by a factor of

$$G_{\rm S}=G_{\rm R}/G_\sigma. \tag{20}$$

Clearly, when $\sigma_{\rm signal}$ is negligible, $G_\sigma\approx 1$ [see Figs. 4(b) and 4(c)]. Then, experimental data are fitted using Eqs. (18)–(20) with the results displayed in Fig. 4.

Authors' Contributions

K.X. and J.-S.T. conceived the original idea and the research. K.X. and J.-S.T. co-supervised the project. L.-Q.X. conducted the experiment and data acquisition, and performed data analysis with the help of K.X. and J.-S.T. W.L. and Y.-Q.L. refined the idea. Y.-P.R., H.Zh., Y.J., H.-D.W. and Y.-Q.L. helped conduction of the experiment.

K.X., J.-S.T., and L.-Q.X. built the theoretical model for interpretation of experimental results. K.X. contributed to the presentation of physics and strengthened the theoretical model. All authors contributed to discussion of experimental results and manuscript writing.

Data Availability

The data that support the plots within this paper are available via figshare at https://doi.org/10.6084/m9.figshare.32630706. All other data used in this study are available from the corresponding authors upon reasonable request.

Code Availability

The custom codes used to produce the results presented in this paper are available from the corresponding authors upon request.

Competing Interests

The authors declare no competing interests.

Acknowledgments

This work was supported by the Innovation Program for Quantum Science and Technology (Grant No. 2021ZD0301400), the National Natural Science Foundation of China (Grant Nos. U25A6008, 92365107, 12674601, 12305020, 12334012, 62575225, 12234012, and 52327808), the National Key R&D Program of China (Grant Nos. 2019YFA0308700, 2019YFA0308704, 2021YFA0718300, 2021YFA1400900, and 2024YFF0726700), the Program for Innovative Talents and Teams in Jiangsu (Grant No. JSSCTD202138), the Innovation Research Foundation of National University of Defense Technology, the China Postdoctoral Science Foundation (Grant No. 2023M731613), and the Jiangsu Funding Program for Excellent Postdoctoral Talent (Grant No. 2023ZB708).

References

[1] Bender C M 2007 *Rep. Prog. Phys.* **70** 947
[2] Feng L, El-Ganainy R, and Ge L 2017 *Nat. Photonics* **11** 752
[3] El-Ganainy R, Makris K G, Khajavikhan M, Musslimani Z H, Rotter S, and Christodoulides D N 2018 *Nat. Phys.* **14** 11
[4] Özdemir Ş K, Rotter S, Nori F, and Yang L 2019 *Nat. Mater.* **18** 783
[5] Kim C, Lu X, Kong D, Chen N, Chen Y, Oxenlowe L K, Yvind K, Zhang X, Yang L, Pu M, and Xu J 2024 *eLight* **4** 6
[6] Fu X, Hu H, Zhang J, Qi J, Zhang S, Wu Q, Lu Y, Chen Z, Chen J, Yu X, Sun Q, and Xu J 2025 *Light Sci. Appl.* **14** 383
[7] Wiersig J 2014 *Phys. Rev. Lett.* **112** 203901
[8] Liu Z P, Zhang J, Özdemir Ş K, Peng B, Jing H, Lü X Y, Li C W, Yang L, Nori F, and Liu Y X 2016 *Phys. Rev. Lett.* **117** 110802
[9] Miri M A and Alù A 2019 *Science* **363** 7709
[10] Chen W, Özdemir Ş K, Zhao G, Wiersig J, and Yang L 2017 *Nature* **548** 192
[11] Lai Y H, Lu Y K, Suh M G, Yuan Z, and Vahala K 2019 *Nature* **576** 65
[12] Hodaei H, Hassan A U, Wittek S, Garcia-Gracia H, El-Ganainy R, Christodoulides D N, and Khajavikhan M 2017 *Nature* **548** 187
[13] Hokmabadi M P, Schumer A, Christodoulides D N, and Khajavikhan M 2019 *Nature* **576** 70
[14] Wu Y, Liu W, Geng J, Song X, Ye X, Duan C K, Rong X, and Du J 2019 *Science* **364** 878
[15] Park J H, Ndao A, Cai W, Hsu L, Kodigala A, Lepetit T, Lo Y H, and Kanté B 2020 *Nat. Phys.* **16** 462
[16] Chen H Z, Liu T, Luan H Y, Liu R J, Wang X Y, Zhu X F, Li Y B, Gu Z M, Liang S J, Gao H, Lu L, Ge L, Zhang S, Zhu J, and Ma R M 2020 *Nat. Phys.* **16** 571
[17] Takata K, Nozaki K, Kuramochi E, Matsuo S, Takeda K, Fujii T, Kita S, Shinya A, and Notomi M 2021 *Optica* **8** 184
[18] Li A, Wei H, Cotrufo M, Chen W, Mann S, Ni X, Xu B, Chen J, Wang J, Fan S, Qiu C W, Alù A, and Chen L 2023 *Nat. Nanotechnol.* **18** 706
[19] Yu S, Meng Y, Tang J S, Xu X Y, Wang Y T, Yin P, Ke Z J, Liu W, Li Z P, Yang Y Z, Chen G, Han Y J, Li C F, and Guo G C 2020 *Phys. Rev. Lett.* **125** 240506
[20] Mao W, Fu Z, Li Y, Li F, and Yang L 2024 *Sci. Adv.* **10** eadl5037
[21] Li Z, Li C, Xiong Z, Xu G, Wang Y R, Tian X, Yang X, Liu Z, Zeng Q, Lin R, Li Y, Lee J K W, Ho J S, and Qiu C W 2023 *Phys. Rev. Lett.* **130** 227201
[22] Dong Z, Li Z, Yang F, Qiu C W, and Ho J S 2019 *Nat. Electron.* **2** 335
[23] Li W, Liu R, Li J, Zhong J, Lu Y W, Chen H, and Wang X H 2023 *Phys. Rev. Lett.* **130** 143601
[24] Lu Y W, Li W, and Wang X H 2025 *ACS Nano* **19** 17953
[25] Ruan Y P, Tang J S, Li Z, Wu H, Zhou W, Xiao L, Chen J, Ge S J, Hu W, Zhang H, Qiu C W, Liu W, Jing H, Lu Y Q, and Xia K 2025 *Nat. Photonics* **19** 109
[26] Xu J, Mao Y, Li Z, Zuo Y, Zhang J, Yang B, Xu W, Liu N, Deng Z J, Chen W, Xia K, Qiu C W, Zhu Z, Jing H, and Liu K 2024 *Nat. Nanotechnol.* **19** 1472
[27] Kononchuk R, Cai J, Ellis F, Thevamaran R, and Kottos T 2022 *Nature* **607** 697
[28] Wang Z Q, Sun Y M, Hu Y D, Wang Y P, Shen R C, Wu W J, and You J Q 2026 *Nat. Commun.* **17** 3343
[29] Gao T, Estrecho E, Bliokh K Y, Liew T C H, Fraser M D, Brodbeck S, Kamp M, Schneider C, Höfling S, Yamamoto Y, Nori F, Kivshar Y S, Truscott A G, Dall R G, and Ostrovskaya E A 2015 *Nature* **526** 554
[30] Doppler J, Mailybaev A A, Böhm J, Kuhl U, Girschik A, Libisch F, Milburn T J, Rabl P, Moiseyev N, and Rotter S 2016 *Nature* **537** 76
[31] Xia S, Kaltsas D, Song D, Komis I, Xu J, Szameit A, Buljan H, Makris K G, and Chen Z 2021 *Science* **3** 72
[32] Song Q, Odeh M, Zúñiga Pérez J, Kanté B, and Genevet P 2021 *Science* **373** 1133
[33] Zhao X, Wang J, Liu W, Shi L, and Zi J 2025 *Phys. Rev. Lett.* **135** 046203
[34] Li Y, Fan C, Hu X, Ao Y, Lu C, Chan C T, Kennes D M, and Gong Q 2022 *Phys. Rev. Lett.* **129** 053903
[35] Deng W, Zhu W, Chen T, Sun H, and Zhang X 2024 *Sci. Adv.* **10** eadp6905
[36] Wang H, Lai Y H, Yuan Z, Suh M G, and Vahala K 2020 *Nat. Commun.* **11** 1610
[37] Wiersig J 2020 *Nat. Commun.* **11** 2454
[38] Lau H K and Clerk A A 2018 *Nat. Commun.* **9** 4320
[39] Geng Q and Zhu K D 2021 *Photonics Res.* **9** 1645
[40] Ding W, Wang X, and Chen S 2023 *Phys. Rev. Lett.* **131** 160801
[41] Loughlin H and Sudhir V 2024 *Phys. Rev. Lett.* **132** 243601
[42] Zhang M, Sweeney W, Hsu C W, Yang L, Stone A D, and Jiang L 2019 *Phys. Rev. Lett.* **123** 180501
[43] Hashemi A, Busch K, Christodoulides D N, Ozdemir S K, and El-Ganainy R 2022 *Nat. Commun.* **13** 3281
[44] Chu Y, Liu Y, Liu H, and Cai J 2020 *Phys. Rev. Lett.* **124** 020501
[45] Degen C L, Reinhard F, and Cappellaro P 2017 *Rev. Mod. Phys.* **89** 035002
[46] Zhang S, Xiao D, Wang F, Huang R, Yu L, Zhou N, He K, Wu X, Nori F, Jing H, and Zhou X 2026 *Nature* **653** 700
[47] Xiao L, Chu Y, Lin Q, Lin H, Yi W, Cai J, and Xue P 2024 *Phys. Rev. Lett.* **133** 180801
[48] Cetin A E and Altug H 2012 *ACS Nano* **6** 9989
[49] Limonov M F, Rybin M V, Poddubny A N, and Kivshar Y S 2017 *Nat. Photonics* **11** 543
[50] Koshelev K, Lepeshov S, Liu M, Bogdanov A, and Kivshar Y 2018 *Phys. Rev. Lett.* **121** 193903
[51] Feldman N, den Boef A J, Amitonova L V, and Koenderink A F 2025 *Nat. Commun.* **16** 11388
[52] Hsu C W, Zhen B, Stone A D, Joannopoulos J D, and Soljačić M 2016 *Nat. Rev. Mater.* **1** 16048
[53] Yesilkoy F, Arvelo E R, Jahani Y, Liu M, Tittl A, Cevher V, Kivshar Y, and Altug H 2019 *Nat. Photonics* **13** 390
[54] Koshelev K, Kruk S, Melik-Gaykazyan E, Choi J H, Bogdanov A, Park H G, and Kivshar Y 2020 *Science* **367** 288
[55] Zhuang Z P, Zhou X, Zeng H L, Li M Y, Chen Z M, He X T, Chen X D, Zhou L, and Dong J W 2025 *eLight* **5** 13
[56] Sun J, Li F, Yan S, Shuai S, Zhu Y, Wang X, He J, Ni D, Wang L, Lin S, Qiu M, Zhu J, and Wen L 2026 *Nat. Photonics* **20** 818
[57] Hu H, Zhou C, Zhang Y, Hu M X, Peng J, Tang H, Huang L, Liu J, Guan C, Zhu Z, Chen X, Lu W, Li X, Deng Z L, Li G, Shi J, and Qiu C

W 2026 *eLight* **6** 12
[58] Bonus F, Knapp C, Valahu C H, Mironiuc M, Weidt S, and Hensinger W K 2025 *Nat. Phys.* **21** 1189
[59] Siegman A E 1986 *Lasers* (Melville, NY: University Science Books)
[60] Wiersig J 2020 *Photonics Res.* **8** 1457
[61] Dowling J P 1998 *Phys. Rev. A* **57** 4736
[62] Almanakly A, Assouly R, Kang H H, Gingras M, Niedzielski B M, Stickler H, Schwartz M E, Serniak K, Hays M, Grover J A, and Oliver W D 2026 *Phys. Rev. Lett.* **136** 183601
[63] Hall J L, Ye J, and Ma L S 2000 *Phys. Rev. A* **62** 013815
[64] Kim J E and Carosi G 2010 *Rev. Mod. Phys.* **82** 557